frontiers | Frontiers in Materials

TYPE Original Research
PUBLISHED 19 August 2022
DOI 10.3389/fmats.2022.966031

OPEN ACCESS

EDITED BY
Chunguang Yang,
Chinese Academy of Sciences (CAS), China

REVIEWED BY
Shujun Li,
Chinese Academy of Sciences (CAS), China
Junlei Li,
Affiliated Zhongshan Hospital of Dalian University, China
Rui Liu,
Shanghai Jiao Tong University, China

*CORRESPONDENCE
Xinyu Wang,
wangxinyu@jmsu.edu.cn

SPECIALTY SECTION
This article was submitted to Biomaterials, a section of the journal Frontiers in Materials

RECEIVED 10 June 2022
ACCEPTED 01 July 2022
PUBLISHED 19 August 2022

CITATION
Zheng X, Duan F, Song Z, Mo H, Li Z, Song Y, Su Y and Wang X (2022), A TMPS-designed personalized mandibular scaffolds with optimized SLA parameters and mechanical properties.
Front. Mater. 9:966031.
doi: 10.3389/fmats.2022.966031

A TMPS-designed personalized mandibular scaffolds with optimized SLA parameters and mechanical properties

Xiaoxiao Zheng[1,2], Feng Duan[1,2], Zhenyu Song[2], Hongbing Mo[2], Zhehao Li[2], Yihan Song[1,2], Yucheng Su[3,4] and Xinyu Wang[1,5]*

[1]Key Laboratory of Oral Biomedical Materials and Clinical Application, Jiamusi University, Jiamusi, China, [2]Experimental Center of Stomatology Engineering, Jiamusi University, Jiamusi, China, [3]Beijing Implant Training College (BITC), Beijing, China, [4]Dental Implant Center, Peking Union Medical College Hospital, China Academy of Medical Science, Beijing, China, [5]Key Laboratory of Microecology-immune Regulatory Network and Related Diseases School of Basic Medicine, Jiamusi University, Jiamusi, China

With the rapid development of 3D printing technology, porous titanium scaffolds have provided a new restoration method to repair bone defects. Compared with the traditional body-centered cubic (bcc) dot matrix structure with a simple arrangement and repetitive structure, the topology-driven properties of triply periodic minimal surfaces (TPMS) can offer a continuous surface and smooth curvature, an excellent platform for cell proliferation. In this study, we used reverse engineering techniques to model the mandible. Sheet and solid networks of gyroid structure, the most common type of TPMS, were selected for porous design and then molded using metal 3D printing technology. At the same time, the surface treatment parameters of sandblasted, large-grit, and acid-etched (SLA) were optimized by orthogonal experimental design. Then, the optimized SLA parameter was used to treat the gyroid with 70% porosity. The result showed that reverse engineering reconstructed the TPMS-based mandibular model had good formability. Furthermore, the best surface morphology, wettability, and roughness were obtained for 3D printed Ti6Al4V under the treatment of 80 mesh Al_2O_3, blasting distances of 4 cm, and a 1:1:2 acid ratio. Moreover, the mechanical properties of Sheet-Gyroid and Solid-Gyroid were significantly different at 70% porosity. The porosity of the scaffolds was close to the design porosity after SLA treatment. However, no significant changes were found in its mechanical properties, all matching the mandible's mechanical properties to meet the implantation conditions.

KEYWORDS

triply periodic minimal surfaces, SLA, selective laser melting, orthogonal experimental design, mechanical behavior, bone defects, 3D printing, porous scaffolds

Highlights

1) Personalized porous design of bone defect sites was designed by using TPMS structures.
2) Optimal SLA surface treatment parameters were screened using an orthogonal experimental design for the pre-implantation treatment of 3D printed Ti6Al4V.
3) TPMS porous mechanical parts were processed with the screened SLA parameters to verify whether the mechanical properties match the bone defect site.
4) Our findings provided a new approach to bone defect regeneration.

Introduction

As people's aesthetic requirements increase, it is essential to restore the shape of the mandible, not only the original contour of the face but also the physiological function of the mandible. So, the repair and reconstruction of mandibular defects have been a hot topic of research in oral and maxillofacial surgery. Yet it still relies mainly on host autologous bone grafting to date, which is currently the best method for repairing minor segmental bone defects (Becker et al., 1996). Autologous non-vascularized free fibular grafts are also very common in the oral cavity (Dimitriou et al., 2011). Autologous bone grafting with vascularized is commonly used, but its surgical damage is more significant (Wei et al., 2016). Therefore, a bionic substitute of natural bone for bone grafting is now generally considered a more desirable treatment. Recent advances in tissue engineering techniques and personalized manufacturing (Zhu et al., 2016) hold promise in this setting.

Three main elements of tissue engineering are bone scaffolds, bone marrow mesenchymal stem cells (BMSCs) and induction factors (Zha et al., 2021). This study focuses on bone scaffolds, for which a variety of personalized scaffolds are available for the repair of mandibular defects (Milovanovic et al., 2020). However, none of the existing repair solutions achieves an ideal mandibular morphology, and mechanical properties are still to be improved. Ideal reconstruction of mandibular defects requires a complex curved restoration that conforms to the original form and restores function and good biomechanical compatibility with the remaining bone tissue. With the development of computer-aided design (CAD), computer-aided manufacturing (CAM) and 3D printing technology, it is possible to mimic the internal three-dimensional structure of the jaw anatomy and the external spatial shape, from microscopic to macroscopic structures, to meet the needs of individualized restorations (Tack et al., 2016; Memon et al., 2020).

The development of reverse-engineering techniques (Fucile et al., 2019) has made it possible to design scaffolds close to the shape of the original host bone defect. Therefore, the design of bone scaffolds focuses on mimicking the original morphology as closely as possible to reduce stress shielding and thus prolong service life. The morphological design of scaffolds has moved from solids that would lead to stress shielding into the era of porosity. However, the restoration designs of the porous scaffolds are very complex. Structures based on simple cubic struts are among the most commonly used in 3D printed tissue engineering scaffolds, and this arrangement leads to severe anisotropy. Anisotropic structures are stiff in the axial direction and weak in the diagonal direction. They are considered detrimental in bone tissue engineering, especially when used as a load-bearing bone site (Pei et al., 2017; Zhang et al., 2018).

Recently, research interest has focused on triply periodic minimal surfaces (TPMS) designs due to their unique mechanical and biological characteristics (Yoo, 2011; Yoo, 2012; Walker et al., 2017). TPMS describes the scaffold's structure through mathematical functions. By adjusting its parameters, the pore parameters can be adjusted to achieve changes in the structural and mechanical properties of the scaffold. Compared to conventional dot-matrix structures, the TPMS method produces a continuous surface structure that is inherently topologically optimized and provides better self-support during selective laser melting (SLM) processing (Lu et al., 2020). TPMS scaffolds have a very high surface area to volume ratio, and this high specific feature of TPMS scaffolds helps to enhance cell adhesion, migration, and proliferation (Yoo, 2014). Many cellular and biological functions, such as ion exchange, oxygen diffusion and nutrient transport, occur on its surface (Pei et al., 2020). Therefore, TPMS scaffolds provide better biological signaling platforms for cells cultured on them. In addition, the infinitely continuous surface with smooth joints ensures fewer stress concentrations and higher mechanical properties than a regular lattice structure support. TPMS function enables a more straightforward implementation of structural parameter variations (Al-Ketan and Abu Al-Rub, 2021), overcomes the drawbacks of traditional truss cell structure design and allows automatic acquisition of digital models of porous bone support with complex microstructures and high-quality surfaces.

To enable good osseointegration of the metal scaffolds after implantation and facilitate osteoblasts' adhesion, proliferation, and differentiation, sandblasted, large-grit, and acid-etched (SLA) (Chambrone et al., 2015), anodizing (Ross and Webster, 2013), micro-arc oxidation (Zhang et al., 2021), and SLActive (Chambrone et al., 2015) surface treatment technologies for titanium alloys are proposed. The SLA forms a surface with a certain number of nested pores, which increases the microscopic surface area of the material and facilitates the mineralization of the extracellular matrix and the differentiation of osteoblasts in contact with the surface. At the same time, SLA as a treatment for cell growth scaffolds increases the adhesion between tissue and material. Further, the nanoscale morphology facilitates the synthesis and adsorption of specific proteins in the extracellular matrix, promoting cell adhesion (Kohal et al., 2013).

In biomedical applications, particularly in artificial implants, a combination of appropriate porous materials, porous structures, and

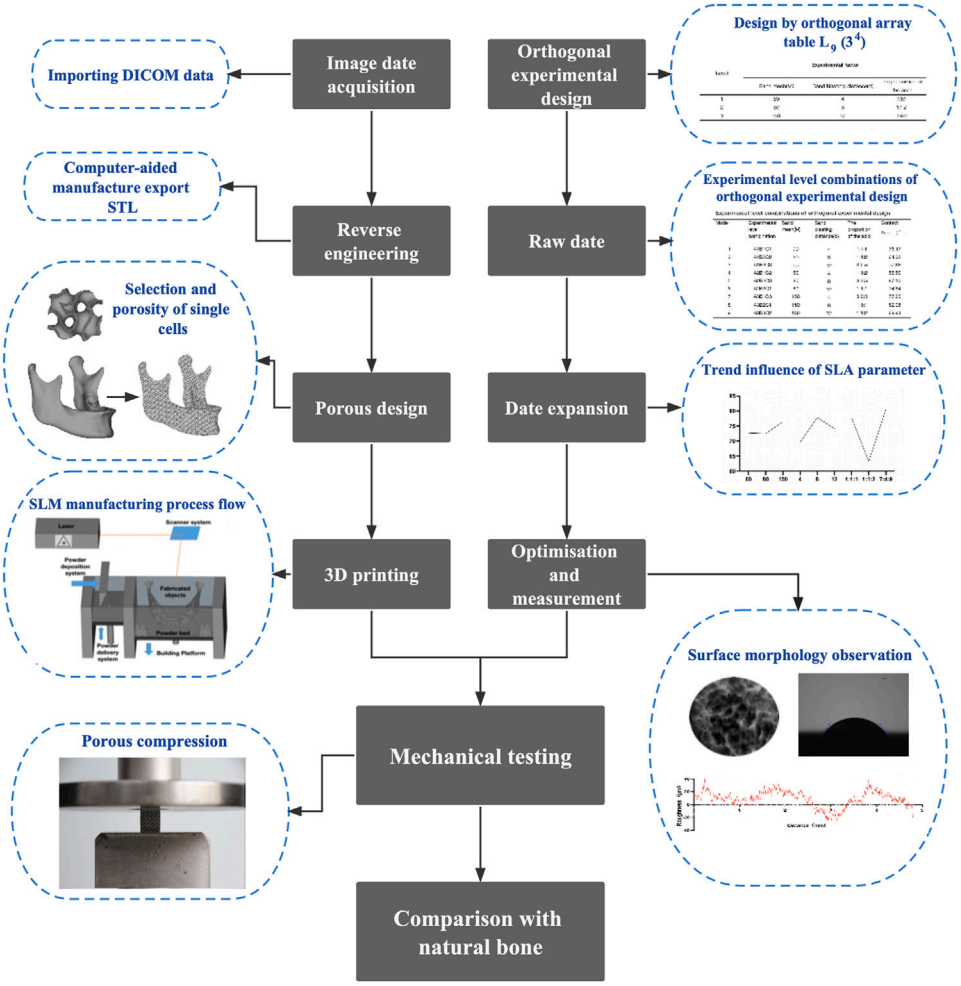

FIGURE 1
Flow chart of the experimental design.

optimum parameters can reduce the elastic modulus of the implant, thus overcoming the stress shielding effect and preventing loosening of the implant (Arabnejad et al., 2016). Optimized morphological parameters, such as pore size and porosity, are also essential to ensure the success of bone implants. For ideal osseointegration, the optimum porosity should exceed 60%. Furthermore, the pore size should be between 600 and 900 μm (Zaharin et al., 2018; Pei et al., 2020). Yan et al. (2015) customized the TPMS scaffolds with SLM to match the elastic modulus of human bone, thus avoiding stress shielding of the implant and improving its durability. Melchels et al. (2010) designed TPMS scaffolds with gyroid on which BMSCs were grown. The results showed that the TPMS scaffolds had a greater cell density and cell distribution than scaffolds prepared by traditional salting. And its permeability was improved by a factor of 10. Lan Li et al. (2019) implanted the 3D printed P-structured TPMS metal scaffolds into the mini-pigs tibia and explored the osseointegration ability of TPMS-based bone substitutes for the first time in an *in vivo* study, confirming the potential of TPMS-based bone substitutes in bone tissue repair.

In this research, 3D printed Ti6Al4V scaffolds with 70% porosity based on the gyroid structure design in TMPS were printed to investigate the relationship between the sheet and solid networks. The optimum parameters for SLA surface treatment were selected by orthogonal experiment design. After SLA treatment, the Sheet-Gyroid and Solid-Gyroid scaffolds were verified to be in good accordance with the requirements for human mandibular implantation through porous mechanical compression testing.

Materials and methods

Figure 1 shows the main flow of this experiment. First, reverse engineering techniques reconstruct the imaging data in

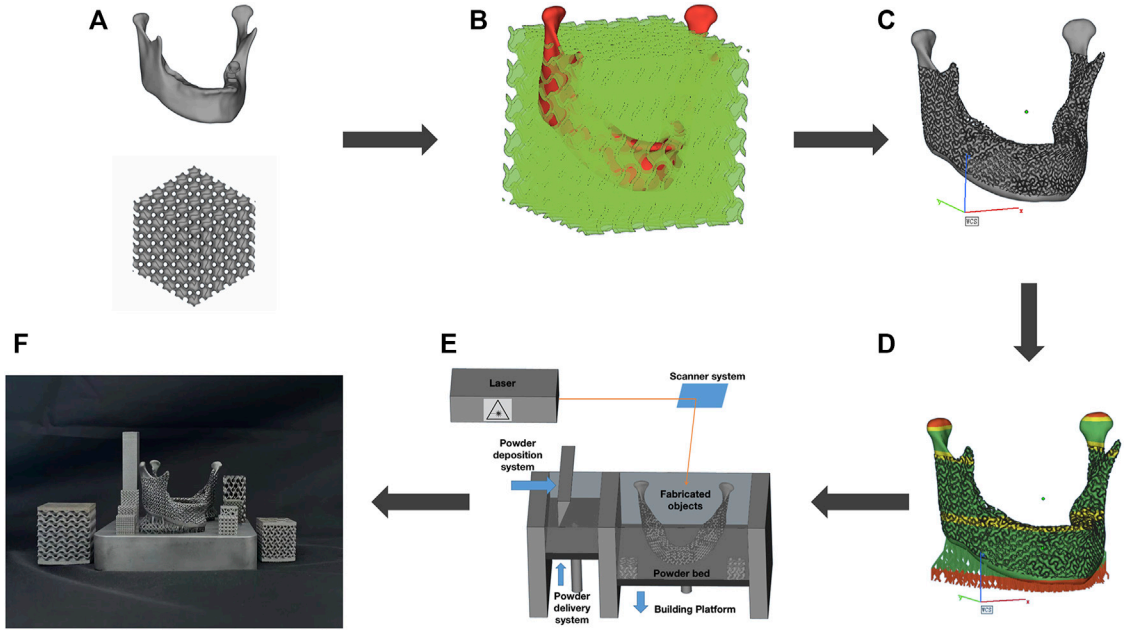

FIGURE 2
TPMS design and 3D-printing. **(A)** Reverse engineering to extract target models; **(B)** Boolean operations; **(C)** Personalized design; **(D)** 3D printing risk analysis; **(E)** SLM fabrication process; **(F)** Print completion.

three dimensions. An orthogonal experimental design was performed to screen the optimal SLA approach. After that, mechanical tests were carried out on the SLA-treated TPMS. And the results were compared with that of the normal bone to determine if its mechanical properties were compatible with the normal mandible.

Personalized TPMS scaffolds design and 3D printing

Scaffolds design

The design is simplified, as shown in Figure 2, and the study is approved by Jiamusi University stomatological hospital ethics committee (NO.2022-KQYY-XS-06), and the volunteer and his family members signed informed consent. The image was scanned by the cone-beam computed tomography (CBCT; Dentsply Sirona, Germany) at 85 kV and 6 mA, 11 × 10 cm field of view (FOV), voxel size of 0.16 mm for 14.4 s, and the scans were saved in Digital Imaging and Communication in Medicine (DICOM) file format.

In reverse engineering, as shown in Figure 2A, the mandibular DICOM file was threshold segmented using Mimics 19.0 software (Materialise, Belgium), 3D-reconstructed, smoothed, and denoised to create customized models of bone defects such as whole mandible, half mandible, and partial mandible. Data was saved in the standard triangular language (STL) file format.

The STL data was then entered into MSLattice software (New York University Abu Dhabi, Abu Dhabi), based on the principle of Boolean operations shown in Figure 2B. The gyroid structure in TPMS with a unit cell size of 2 mm, a porosity of 70%, and a mesh density of 30 points was selected. It is important to note that during mandibular re-placement surgery or arthroplasty, the subarticular cavity was opened; the condyle should be solidified to avoid soft-tissue growth during the healing process. In this research, an interconnected biomimetic porous TPMS structure was designed, and their relationship was sheet networks and solid networks, as shown in Figure 3B.

2 mm supports were generated in Magics 26.0 software (Materialise, Belgium), as shown in Figure 2C, and fitted with superstructure adjustment coordinates. Then, the file was subjected to a print risk analysis, as shown in Figure 2D. Once the analysis was complete, slicing was carried out with a slice thickness of 0.025 mm, and a Concept Laser Slicer (CLS) format file was exported as a print prep file and then transferred to a 3D printer (Figure 2E).

3D printing and post-processing

The Mlab cusing 100R (Concept laser, Germany) was used to produce the personalized scaffolds and rectangular mechanical specimens, as shown in Figure 3A. Furthermore, the Ti6Al4V powder (Concept laser, Germany) of 10–53 μm was used as printing material. The

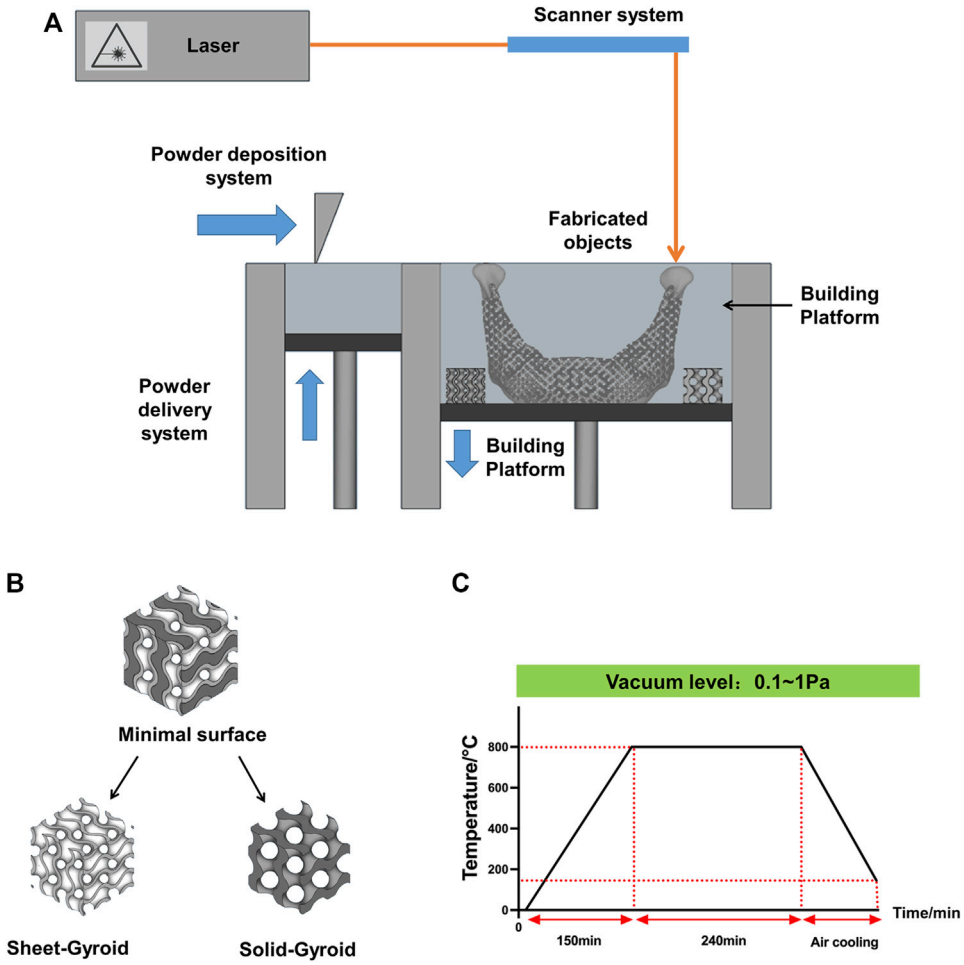

FIGURE 3
(A) Scheme of the SLM process; **(B)** Strategies to create lattices form a minimal surface; **(C)** Heat-treatment process flow chart.

laser emitter melts the powder at a scanning speed of 900 mm s-1 and a layer of 0.025 mm was formed through 50 μm spot diameters at 95 W in the chess scanning pattern. Electron beam scanning was utilized to generate a cross-section layer by fusing the powder. Subsequently, a new layer of powder was applied, and the process was repeated until the whole construct had been built (Figure 2F). All process was under inert gas protection.

To remove stress, enhance the toughness of 3D printed Ti6Al4V specimens and improve their mechanical properties, they had to be heat-treated by a vacuum heat treatment furnace (Beijing Hangxin AM Technology Co. Ltd., China). Firstly, vacuum circumstance was achieved by vacuum pumping for 10 min (vacuum degree below 1 Pa). A temperature of 800 °C was achieved at 150 min under a vacuum state and preserved for 240 min. Then with the air cooling to 150 °C, open the chamber and remove the specimens. The heat treatment process is shown in Figure 3C.

Orthogonal experimental design and optimization analysis

SLA's surface morphology and contact angle are affected by various factors, including the blasting distance, grit mesh, proportion of the acid, blasting angle, blasting time, acid etching time, and temperature (Rupp et al., 2004). Based on the results of previous exploratory experiments and the surface treatment methods used as previously described (Perrin et al., 2002), the controlled temperature of 75°C and reaction time of 30 min were selected for the surface treatment of the 3D printed porous Ti6Al4V scaffolds. Three surface treatment parameters, A (grit mesh), B (sandblasting distance), and C (the proportion of the acid), were chosen as orthogonal experimental factors, Where Al_2O_3 (Beijing Hangxin AM Technology Co. Ltd., China) is chosen as the grit for sandblasting, the ratio of an acid refers specifically to the ratio of sulfuric acid (Tianjin Kaitong Chemical Reagent Co. Ltd., China), hydrochloric acid (Tianjin Kaitong

TABLE 1 Orthogonal experimental design.

Level	Experimental factor		
	Grit mesh	Sandblasting distance	The proportion of the acid
1	60	4	1:1:1
2	80	8	1:1:2
3	150	12	7:4:9

Chemical Reagent Co. Ltd., China) and deionized water (Tianjin Kaitong Chemical Reagent Co. Ltd., China). Three levels were selected for each factor (Table 1), and an orthogonal table $L_9(3^4)$ was selected.

The sample surface morphology was characterized by field emission scanning electron microscopy (FE-SEM; FJEOL, Japan). The biocompatibility of 3D-printing Ti6Al4V scaffolds is directly related to their surface wettability (Yu et al., 2020). The contact angle is an important feature in determining materials' wettability. The smaller the intact angle is, the better the wettability is. Two microliters of deionized water were dropped onto the sample's surface after the spread was completed, and the contact angle was detected using a contact angle goniometer (Power each, China), The droplet image was captured and frozen for angle measurement. And we measured surface roughness with a compact roughness measuring instrument MarSurf PS10 (Mahr GmbH, Germany). Its maximum measuring range is 350 μm (−200 μm to +150 μm).

According to the orthogonal experimental design, nine groups of experimental level combinations (the combinations of surface treatment parameters) were determined. The impact of different SLA parameters on the contact angle was determined and put in order through orthogonal experimental optimization analysis, and an optimal combination was then obtained.

Porosity measurement and mechanical properties of TPMS

Porosity

Porosity is measured by weight and drainage methods. In the weight method, M_a and M_{theory} is the weight of the specimens in air and the theoretical weight of Ti6Al4V, the porosity 'P' was calculated with the equation

$$P = 1 - \left(\frac{M_a}{M_{theory}}\right) \times 100\%$$

Another method is the drainage method, where the suspension derives the object's mass in water 'M_w'. The ρ_{water} and ρ_{theory} are the density of water, and Ti6Al4V is 1 g cm-3 and 4.41g cm-3, respectively. And the porosity is calculated according to the buoyancy of the specimens.

$$P = \frac{\frac{M_a \times \rho_{water}}{M_w}}{\rho_{theory}} \times 100\% = \frac{M_a}{4.41 \times M_w} \times 100\%$$

Design porosity can be derived directly from CAD software.

Mechanical properties

Porous rectangular specimens were subjected to a quasi-static compressive test using a Universal tester Machine (Jinan Heng Rui Jin Testing Machine Co., Ltd., China). According to ISO13314:2011 standard (Standard, 2011), porous rectangular specimens (Sheet-Gyroid or Solid-Gyroid structures; length: 12 mm, width:10 mm, with one 0.5 mm rectangular sheet on both ends to avoid stress concentrations during the 3D printing process and the removal of supports after printing; five rectangular specimens for each type) before and after SLA were compressed at a head speed of 1.2 mm min-1. The compression stop condition is compressed until the displacement is 8 mm or the force reaches 99 KN.

In this study, elastic modulus (E) was defined as the slope of the stress-strain curve within the elastic deformation region, offset yield strength (σs) was set at compressive 0.2% offset stress, and compressive strength (σbc) was determined as the first local maximum in the stress-strain curve.

Result

Orthogonal experimental design results

First, we measured the contact angle and observed the SEM. The contact angle of the 3D printed titanium samples is shown in Table 2. Among the nine groups, the highest contact angle was 82.24° (group $A_2B_2C_3$, Figure 4E), and the lowest value was 54.55° (group $A_2B_1C_2$, Figure 4D). According to these results, minor variations in surface treatment parameters of the SLA could lead to a significant change in contact angle (the maximum change value was 27.69°), indicating the significance of the surface treatment method.

TABLE 2 Experimental level combinations of orthogonal experimental design.

No.	Experimental level combination	Grit mesh	Sandblasting distance	The proportion of the acid	Contact angle (°)
1	$A_1B_1C_1$	60	4	1:1:1	75.37
2	$A_1B_2C_2$	60	8	1:1:2	64.03
3	$A_1B_3C_3$	60	12	7:4:9	77.72
4	$A_2B_1C_2$	80	4	1:1:2	54.55
5	$A_2B_2C_3$	80	8	7:4:9	82.24
6	$A_2B_3C_1$	80	12	1:1:1	73.74
7	$A_3B_1C_3$	150	4	7:4:9	77.66
8	$A_3B_2C_1$	150	8	1:1:1	81.66
9	$A_3B_3C_1$	150	12	1:1:2	69.94

Analysis of the SEM of these nine groups of samples shows that as the concentration of hydrochloric acid decreases, grit residues from sandblasting begin to appear. In the third group, residual sandblasted particles can be observed in Figure 4C. Their grits are proven to affect osseointegration (Pei et al., 2020) and need to be removed prior to implantation. As shown in Table 2, the contact angle was also larger in these groups than in the remaining two groups.

The contact angle range of nine surface treatments was analyzed. Table 3 presents the results of the orthogonal experiment design, in which K represents the mean of the contact angle for the same experimental factor at the same level. The range was calculated by using the following formula:

$$R = max_k - min_k$$

where R represents the range of the same experimental factor. In other words, R is the extreme difference of the same factor.

According to the results of the range analysis of the orthogonal experimental design, the greater the R was, the more significant their influence was. The proportion of the acid had the most significant effect, followed by the sand mesh. In contrast, the sandblasting distance had the slightest effect. Through the range analysis (Figure 5), the optimal SLA parameters for the 3D printed Ti6Al4V were $A_2B_1C_2$. Specifically, the optimal SLA parameters were 80 mesh Al_2O_3, blasting distance of 4 cm, and the proportion of the acid of 1:1:2.

Verification of the optimized SLA parameters derived from the orthogonal experimental design

To verify the optimization results, we repeated the experiment. SEM results showed that the sandblasting process formed irregular pits and many sharp protrusions with several tens of microns on the surface of the specimens. This caused partial exfoliation of the substrate (Figures 6B,E). Compared with Figures 6A,D, sandblasting removed the half-melted powder during the additive fabrication process and residual titanium alloy powder, which could not be removed by simple cleaning and is harmful to implantation (Wang et al., 2017; Song et al., 2019). So, the surface matrix exfoliation and grit residue due to sandblasting require further acid etching to remove.

Figure 6C showed that the simple sandblasting treatment creates an irregular surface roughness of several tens to hundreds of microns, and they were the first surface roughness level. Upon further magnification (Figure 6F), the treated sample's surface forms a pore-like roughness with a micro-nano composite. Further magnification can be observed that there are also many small pore structures of several microns in size within the large pores. There were some nano-convex structures within these tiny pores, which were the tertiary pores formed by the surface treatment.

Results also demonstrated that the surface contact angle of the SLA optimized specimens was 53.07° (Figure 6I). The surface contact angle of the sandblasted specimens was 49.98° (Figure 6H), both of which were statistically significant compared to the surface contact angle of the untreated specimens of 80.25° (Figure 6G), indicating that the SLA treatment can increase the surface hydrophilicity. Compared with the samples only treated by sandblasting, SLA treatment slightly increased the contact angle (Figure 6K).

The roughness of the surface is presented in Figures 6J,L, l. Both the SLA treatment and the sandblasting treatment reduced the surface roughness. The roughness was significantly lower in the sandblasted group (R_a = 2.66 μm, R_q = 3.36 μm) and SLA group (R_a = 3.37 μm R_q = 4.24 μm) only compared to the untreated group (R_a = 7.97 μm, R_q = 9.73 μm). An ideal roughness should be between 1–10 μm (Yu et al., 2020), both treatments resulted in roughness within this range.

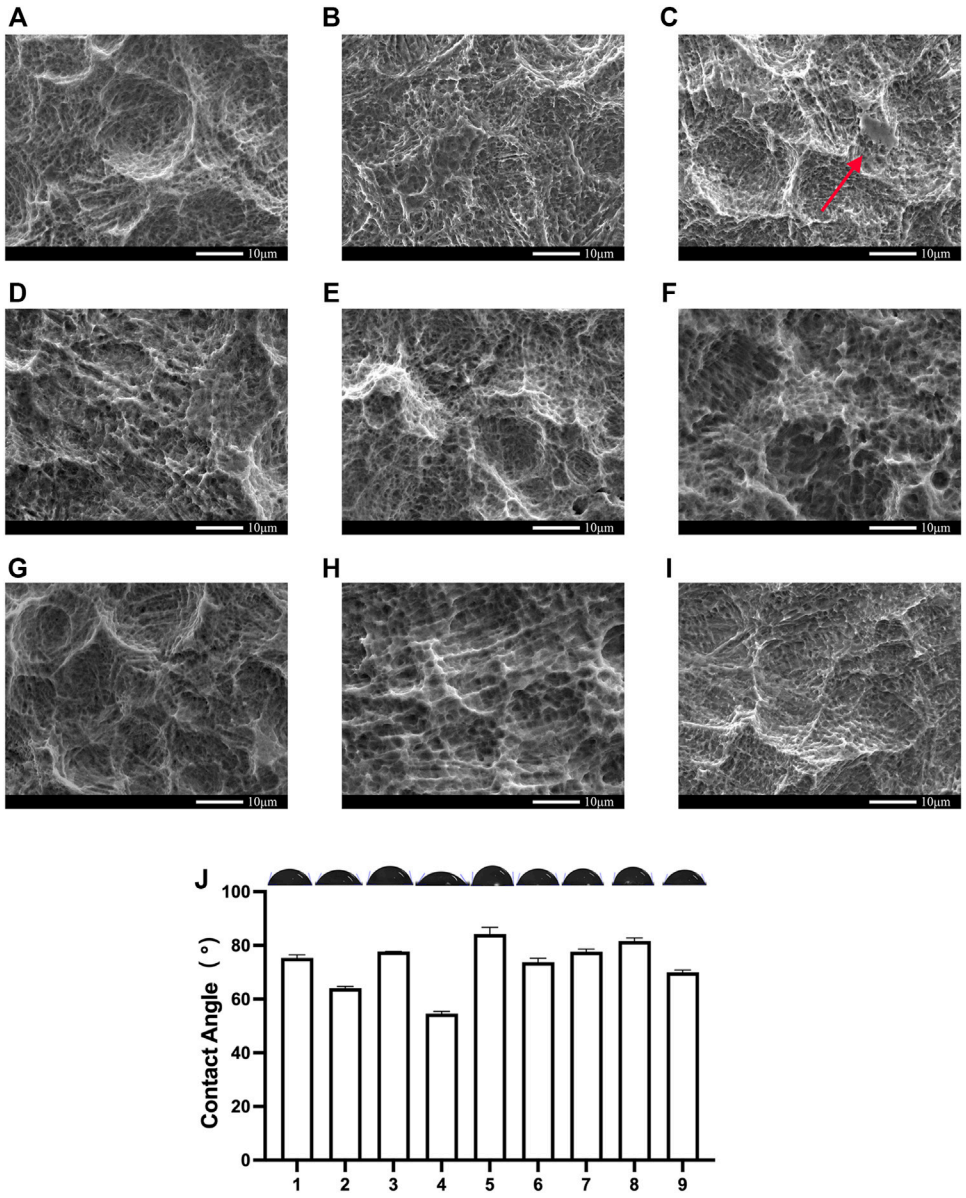

FIGURE 4
SEM and contact angle of the Orthogonal experimental design. **(A)** group;**(B)** group;**(C)** group;**(D)**The group;**(E)**The group;**(F)**The group;**(G)** The group;**(H)**The group;**(I)**The group; **(J)**The contact angle of the Orthogonal experimental design. Error bars represent means ± SD and specimens number $n = 3$.

Porosity test results

After 3D printing, the porosity was measured and presented in Table 4. Generally, as-built specimens' porosities were 15% lower than designed porosity. After surface treatment, porosity increased and approached the designed value. There was no statistical significance between porosity measurement by weight method and drainage method.

Mechanical properties results and comparison with bone defect sites

Sets of compressive stress-strain curves of Sheet-Gyroid and Solid-Gyroid structures before and after SLA treatment are depicted in Figure 7A, respectively, and their strain pictures under compression (Figure 7B). The specimens cracked along a 45-degree highly stressed band where the red color indicates, and

TABLE 3 Optimization of the results of the orthogonal experimental design.

No.	Experimental factor				Contact angle (°)
	A	B	C	D	
1	1	1	1	1	75.37
2	1	2	2	2	64.03
3	1	3	3	3	77.72
4	2	1	2	3	54.55
5	2	2	3	1	82.24
6	2	3	1	2	73.74
7	3	1	3	2	77.66
8	3	2	1	3	81.66
9	3	3	2	1	69.94
K1	72.373	69.193	76.923	—	—
K2	70.177	75.977	62.840	—	—
K3	76.420	73.800	79.207	—	—
Range R	6.243	6.784	16.367	—	—
Ranking	C > B > A	—	—	—	—
Optimal level	A2	B1	C2	—	—

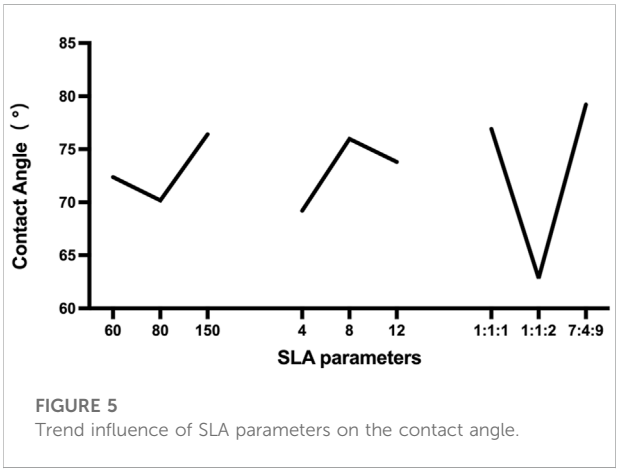

FIGURE 5
Trend influence of SLA parameters on the contact angle.

all the structures tend to present a severe drop in strength associated with shear collapse.

SLA removed the remaining unmelted particles on the surface, weakening the specimen's strength, but not statistically significant, as shown in Figures 7C–E. From Table 5, the effect on mechanical properties before and after surface treatment was insignificant. The yield strength of the Sheet-Gyroid decreased only 15.37 MPa, and compressive strength decreased only 17.15 MPa. In contrast, the yield strength of Solid-Gyroid decreased only 10.36 MPa, and compressive strength decreased only 12.85 MPa. Both were not statistically significant, proving that SLA treatment could increase the porosity without affecting the mechanical properties. This result was certainly good news for the subsequent clinical implantation of TPMS, as we hope to have the best mechanical properties while obtaining a higher specific surface area. We also found that the mechanical properties of the Sheet-Gyroid were better than those of the Solid-Gyroid in all cases. The elastic modulus of gyroid without SLA decreased from sheet to solid by 1.09 GPa, and the yield and compressive strength decreased by 79.81 and 96.22 MPa, respectively. After SLA, The Sheet-Gyroid and the Solid-Gyroid elastic module decreased by 1.36 GPa, and the yield and compressive strength decreased by 74.8 and 91.92 MPa, respectively.

To make metal scaffolds to be suitable for replacing natural bone, their mechanical properties must match that of the normal bones. The material's mechanical strength can be easily manipulated by changing equation. A comparison of the elastic modulus of all porous structures was performed with that of natural bone. The mechanical properties of the porous scaffold had to be within the range of that of the normal bone to avoid stress shielding. The modulus of elasticity of cortical bone and cancellous bone are 4–30 MPa and 0.2–2 GPa (Li et al., 2014), respectively, and the modulus of elasticity of the human mandible is 0.56–12.7 GPa (Novaes et al., 2010). All specimens in this experiment had a modulus of elasticity within the range. Another factor to be considered when selecting a suitable porous structure is the yield strength of the sample. The yield strength of natural bone is reported in the literature to be between 20–193 MPa (Li et al., 2014). All specimens were within the required yield strength range except for the untreated Sheet-Gyroid group in this experiment (Figure 7F). The individual values were slightly higher than the yield strength of natural bone, but the average values were still within the required range (Figure 7G).

Discussion

Porous structures have many application scenarios in the field of bone tissue regeneration (Guvendiren et al., 2016; Jammalamadaka and Tappa, 2018). Yet, the performance of porous structures designed by existing techniques in cell adhesion and proliferation is not ideal, mainly due to their unsmooth surfaces (Pei et al., 2020). Researchers have found that TPMS has the property of generating continuous surface and smooth curvature, hence, we adopted TPMS to design porous supports in this paper. In the fabrication of porous structures, 3D printing has its unique advantages because of its ability to precisely control cytoskeletal elements such as pore size, trabeculae, and wall thickness of porous structures. In addition, 3D printing can meet the needs of individual designs. In this study, we used reverse engineering techniques to extract the mandibular model, completed the porosity design based on the TPMS functions, and finally, the product molding

10.3389/fmats.2022.966031

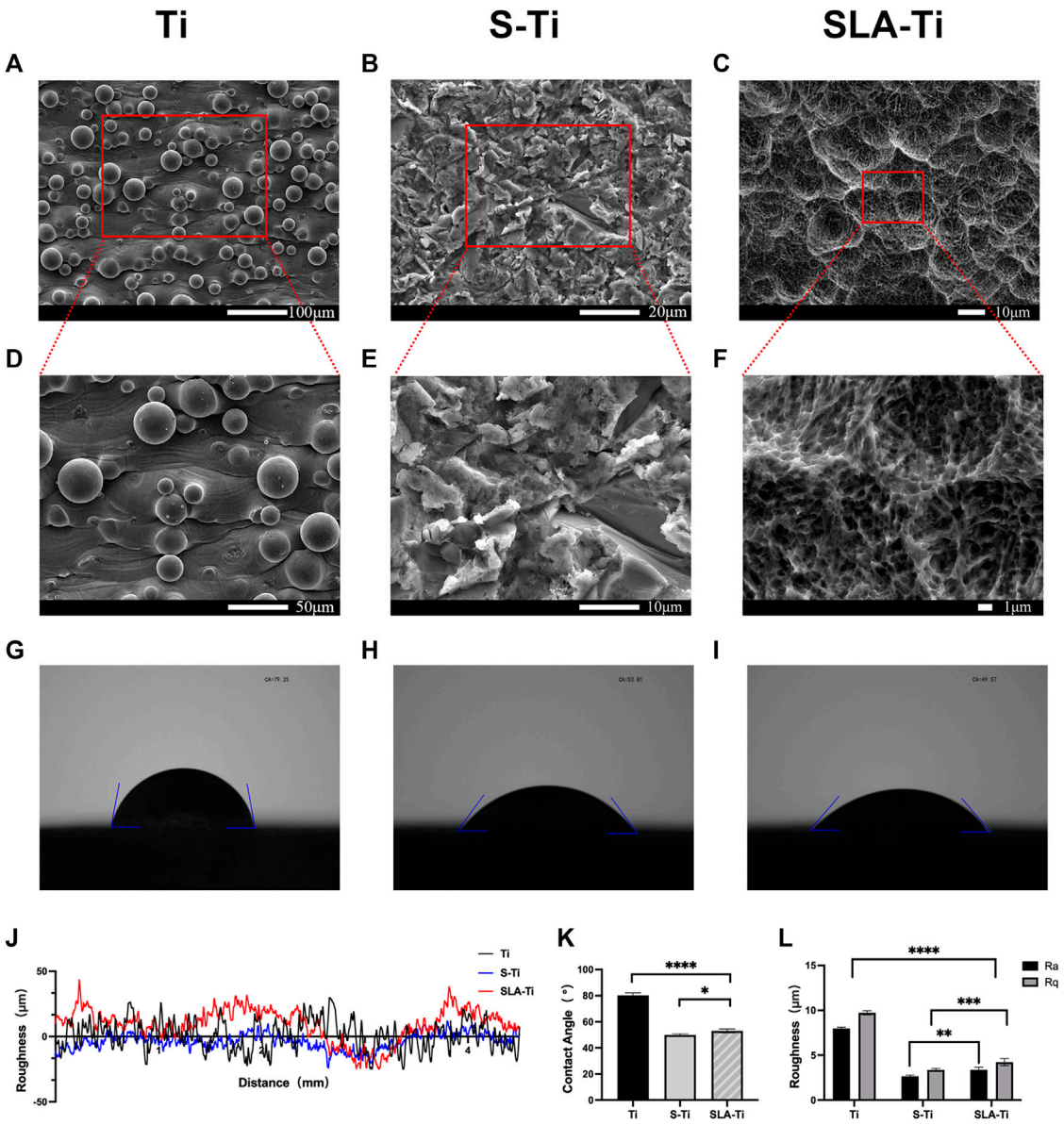

FIGURE 6
SEM images of Ti **(A, D)**, S-Ti **(B, E)**, and SLA-Ti **(C, F)**; water contact angles of Ti **(G)**, S-Ti **(H)**, and SLA-Ti **(I)**; **(J, L)** Surface roughness of Ti, S-Ti and SLA-Ti; **(K)** contact angles of Ti, S-Ti and SLA-Ti. Error bars represent means ± SD and specimens number n = 5.

TABLE 4 Pore characterization of the porous structure.

	Design porosity (%)	Weight method		Drainage method	
		As-built porosity (%)	Post-SLA porosity (%)	As-built porosity (%)	Post-SLA porosity (%)
Sheet-Gyroid	70	55.26	66.18	56.03	67.69
Solid-Gyroid	70	57.37	70.08	56.87	69.65

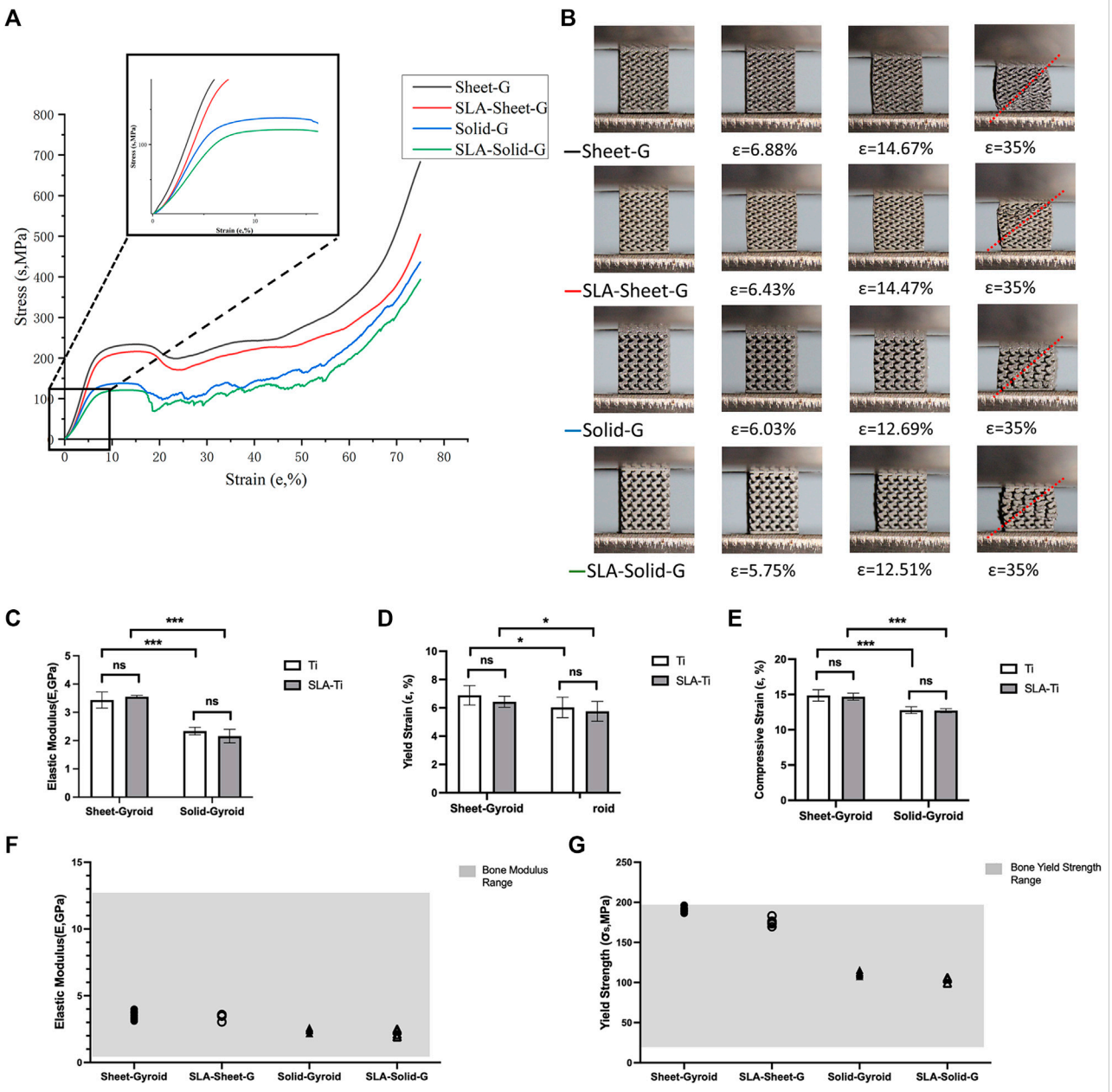

FIGURE 7
(A) Compressive stress-strain curves of Sheet-Gyroid and Solid-Gyroid structures before and after SLA; **(B)** Pictures of the corresponding strain from the compression; Elastic Modulus **(C)**, corresponding yield strain **(D)** and corresponding compressive strain **(E)** of Sheet-Gyroid and Solid-Gyroid before and after SLA. Comparison between numerical and experimental elastic modulus **(F)** and yield strength **(G)** for Sheet-Gyroid and Solid-Gyroid samples before and after SLA in the range of bone modulus. Error bars represent means ± SD and specimens number n = 5.

was carried out by 3D printing. Meanwhile, we performed an orthogonal experimental design to filter and optimize the SLA parameters. Surface treatment of 3D printed Ti6Al4V scaffolds was carried out, and porous compression experiments were conducted to evaluate its mechanical properties. The results demonstrated that the porous scaffold matched well with the mechanical properties of the bone and met the implantation criteria.

In the metal additive manufacturing process, the TPMS-based printed product was slightly different from the designed one. We believed that the melt pool's temperature and geometry affected the products' density, ultimately leading to the difference

TABLE 5 Results of static compressive tests.

		Elastic modules (E,GPa)	Yield strength (σs,MPa)	Compressive strength (σbc,MPa)
Sheet-Gyroid	Ti	3.43 ± 0.28	192.17 ± 2.84	233.44 ± 2.37
	SLA-Ti	3.55 ± 0.05	176.80 ± 3.72	216.29 ± 2.92
Solid-Gyroid	Ti	2.34 ± 0.13	112.36 ± 2.42	137.22 ± 1.33
	SLA-Ti	2.16 ± 0.24	102.00 ± 3.06	124.37 ± 2.44

between the as-built products and the design. The main parameters affecting the temperature and geometry of the melt pool are the layer thickness, scanning speed, laser power, hatch distance, and spot diameters (Casati et al., 2016). The Mlab series we chose in this paper was an SLM device with minor spot diameters on the market. Therefore, we should optimize the parameters other than the spot diameters, such as scanning speed, layer thickness and hatch distance, by controlling the energy density formula to improve the printing accuracy. In addition, by observing the gyroid structure, we found powder staining at the interface between its parallel and lower surfaces, which was due to the limited heat dissipation during the printing process (Vaithilingam et al., 2016). This reason caused the half-melted powder to remain on the porous support, which may also be one of the reasons for the difference between the product and the design.

To solve the limited heat dissipation during the 3D-printing process mentioned above, we usually need to add additional supports to enhance heat dissipation. Supports can be divided into solid and non-solid supports. Solid supports are responsible for anchoring the part, and non-solid supports safeguard the quality of the lower surface of the part. However, we found that the SLM-printed gyroid structure met the requirement of self-supporting. The tilt angle of each layer was less than 45°, which further validated that SLM technology was suitable for printing gyroid structures.

Reportedly, the TPMS surpasses conventional porous titanium scaffolds in several aspects. First, although the mechanical properties of the conventional cube structures are slightly better than those of the gyroid structures, only the cube porous structures with a pore size of 0.3–0.5 mm are suitable for implant application according to implantation young's modulus (Zaharin et al., 2018). In contrast, the gyroid structures for implant application have a more comprehensive range of pore sizes. Secondly, the mechanical properties of this paper's 70% gyroid structures were better than those of the Voronoi structures but worse than those of the gradient varying Voronoi structures (Wang et al., 2018). Finally, when compared with the diamond structure in TPMS, the gyroid exhibits better performances than the diamond in terms of the elastic modulus, ultimate strength and ductility (Liu et al., 2020).

As we all know, porous structures' mechanical properties have different applications in different fields (Wang et al., 2018). When the porous structure is used as a load-bearing structure, the porous structure mainly works in the elastic phase and yield phase, and the focus is on the elastic modulus and yield stress of the porous material; when the porous structure is used as an impact-resistant material, the porous structure mainly works in the platform phase and densification phase. The maximum compressive strength of the porous material is crucial for its function. Relatively speaking, the performance in the elastic phase is of more interest for biological scaffolds. The elastic modulus needs to match the human bone to reduce the stress shielding of the implant, and the high yield stress has a positive effect on improving the fatigue resistance of the implant (Liu et al., 2016). According to the Gibson–Ashby model (Gibson, 2005), the porosity of the porous structure can be adjusted to match the actual requirements of elastic modulus and yield stress at the implant site. However, these studies were based on porous structures of the same unit cell size. They did not consider the effect of pore size variation on mechanical properties. In this paper, we confirmed whether there was no significant difference in mechanical properties between sheet networks and solid networks for TMPS, including elastic modulus and yield strength, which provides a new consideration for the design of scaffolds.

According to the above discussion of porous structure mechanical properties, we can reversely model the bone defect site preoperatively and match the mechanical properties with it during the porosity design of the porous scaffolds. For example, the mechanical properties of the defect site can be matched by changing the unit cell size and porosity and selecting different TPMS structures as well as sheet networks or solid networks in MSLattice software (Al-Ketan and Abu Al-Rub, 2021). Then, we consider using Finite Element Analysis (FEA) simulated the forces in the natural bone. The pre-process for the implant can be performed if the mechanical properties match the implantation criteria. If not, the mechanical properties can be fine-tuned by changing these four parameters for further optimization.

We also found that the SLA treatment formed a multi-level pore structure on the surface of the titanium alloy. Also, enhanced hydrophilicity and reduced roughness were observed. Among the pore structures, the formation of the first-class structure was caused by the local stress concentration phenomenon on the surface of the samples during the sandblasting process. These stress concentrations manifest as uneven corrosion during acid etching, where large

craters of several tens of microns formed during the blasting process with large grains of grit, while small pore structures of several microns and nanometers were formed during the acid etching process (Xing et al., 2014). To be specific, the acid etching process can not only form a multi-level hole structure on the highly irregular surface after sandblasting, release the local stress concentration caused by sandblasting, pin down the sharp peaks formed after sandblasting, but also remove the residual sandblasting grit on the surface of the substrate after sandblasting (Stepanovska et al., 2020). In addition, according to the results of orthogonal experiments, more sandblasted particles were left on the sample surface when the concentration of hydrochloric acid decreased. According to the literature (Yu et al., 2020), the attachment of more metal powder on the metal surface of 3D-printed titanium alloy may be the reason for the higher R_a and R_q value. Furthermore, the surface chemistry of 3D-printed titanium alloy was changed by acid etching to increase its hydrophilic properties.

The above discussion of this experiment was based on 3D printing, surface treatment and mechanical properties. Based on the present experiments, we will expand the selection of porosity and choose more minimal surface structures to explore the mechanics of TPMS and conduct further cellular and animal experiments to verify its effect on osseointegration. Moreover, we can follow the irregular variation of natural bone and design a porous gradient structure for further study.

Conclusion

The TPMS-based design of the mandible model reconstructed by reverse engineering has good formability. Under 80 mesh Al_2O_3, sandblasting distance of 4 cm and 1:1: 2 acid ratio, the 3D-printed Ti6Al4V resulted in the best surface finish morphology, wettability, and roughness. At 70% porosity, the mechanical properties of Sheet-Gyroid and Solid-Gyroid were significantly different. The SLA treatment resulted in a scaffold with porosity close to the design porosity and had no significant effect on its mechanical properties. The study can be applied not only to the mandible but also to any bone defect in any part of the body by adjusting the parameters. It also provides an idea for SLA surface treatment of metal implants.

Data availability statement

The raw data supporting the conclusion of this article will be made available by the authors, without undue reservation.

Ethics statement

The studies involving human participants were reviewed and approved by the Ethics Committee of Jiamusi University. The patients/participants provided their written informed consent to participate in this study.

Author contributions

Conceptualization: XZ and XW; methodology: XZ; software: XZ; validation: FD and ZS; data curation: HM; writing—original draft preparation: XZ; writing—review and editing: ZL and YS; supervision: YS; and funding acquisition: XW. All authors contributed to the article and approved the submitted version.

Funding

This work was funded by the “Touyan” Project of Heilongjiang Province of China and the National Key Research and Development Program of China (2016YFC1102603).

Acknowledgments

The first author would like to acknowledge the help of Professor Oraib Al-Ketan of New York University Abu Dhabi in certain aspects of the software.

Conflict of interest

The authors declare that the research was conducted in the absence of any commercial or financial relationships that could be construed as a potential conflict of interest.

Publisher’s note

References

Al-Ketan, O., and Abu Al-Rub, R. K. (2021). MSLattice: A free software for generating uniform and graded lattices based on triply periodic minimal surfaces. *Mat. Des. Process. Comms.* 3 (6), e205. doi:10.1002/mdp2.205

Arabnejad, S., Burnett Johnston, R. B., Pura, J. A., Singh, B., Tanzer, M., Pasini, D., et al. (2016). High-strength porous biomaterials for bone replacement: A strategy to assess the interplay between cell morphology, mechanical properties, bone ingrowth and manufacturing constraints. *Acta biomater.* 30, 345–356. doi:10.1016/j.actbio.2015.10.048

Becker, W., Urist, M., Becker, B. E., Jackson, W., Party, D. A., Bartold, M., et al. (1996). Clinical and histologic observations of sites implanted with intraoral autologous bone grafts or allografts. 15 human case reports. *J. Periodontology* 67 (10), 1025–1033. doi:10.1902/jop.1996.67.10.1025

Casati, R., Lemke, J. N., Tuissi, A., and Vedani, M. (2016). Aging behaviour and mechanical performance of 18-Ni 300 steel processed by selective laser melting. *Metals* 6 (9), 218. doi:10.3390/met6090218

Chambrone, L., Shibli, J. A., Mercúrio, C. E., Cardoso, B., and Preshaw, P. M. (2015). Efficacy of standard (SLA) and modified sandblasted and acid-etched (SLActive) dental implants in promoting immediate and/or early occlusal loading protocols: A systematic review of prospective studies. *Clin. Oral Impl. Res.* 26 (4), 359–370. doi:10.1111/clr.12347

Dimitriou, R., Jones, E., McGonagle, D., and Giannoudis, P. V. (2011). Bone regeneration: Current concepts and future directions. *BMC Med.* 9 (1), 66. doi:10.1186/1741-7015-9-66

Fucile, P., Papallo, I., Improta, G., De Santis, R., Gloria, A., Onofrio, I., et al. (2019). "Reverse Engineering and Additive Manufacturing towards the design of 3D advanced scaffolds for hard tissue regeneration," in Proceeding of the 2019 II Workshop on Metrology for Industry 4.0 and IoT (MetroInd4. 0&IoT), Naples, Italy, June 2019 (IEEE), 33–37. doi:10.1109/metroi4.2019.8792891

Gibson, L. J. (2005). Biomechanics of cellular solids. *J. biomechanics* 38 (3), 377–399. doi:10.1016/j.jbiomech.2004.09.027

Guvendiren, M., Molde, J., Soares, R. M., and Kohn, J. (2016). Designing biomaterials for 3D printing. *ACS Biomater. Sci. Eng.* 2 (10), 1679–1693. doi:10.1021/acsbiomaterials.6b00121

Jammalamadaka, U., and Tappa, K. (2018). Recent advances in biomaterials for 3D printing and tissue engineering. *J. Funct. Biomater.* 9 (1), 22. doi:10.3390/jfb9010022

Kohal, R. J., Bächle, M., Att, W., Chaar, S., Altmann, B., Renz, A., et al. (2013). Osteoblast and bone tissue response to surface modified zirconia and titanium implant materials. *Dent. Mater.* 29 (7), 763–776. doi:10.1016/j.dental.2013.04.003

Li, Y., Yang, C., Zhao, H., Qu, S., Li, X., Li, Y., et al. (2014). New developments of Ti-based alloys for biomedical applications. *Materials* 7 (3), 1709–1800. doi:10.3390/ma7031709

Li, L., Shi, J., Zhang, K., Yang, L., Yu, F., Zhu, L., et al. (2019). Early osteointegration evaluation of porous Ti6Al4V scaffolds designed based on triply periodic minimal surface models. *J. Orthop. Transl.* 19, 94–105. doi:10.1016/j.jot.2019.03.003

Liu, Y., Li, S., Wang, H., Hou, W., Hao, Y., Yang, R., et al. (2016). Microstructure, defects and mechanical behavior of beta-type titanium porous structures manufactured by electron beam melting and selective laser melting. *Acta mater.* 113, 56–67. doi:10.1016/j.actamat.2016.04.029

Liu, F., Ran, Q., Zhao, M., Zhang, T., Zhang, D. Z., Su, Z., et al. (2020). Additively manufactured continuous cell-size gradient porous scaffolds: Pore characteristics, mechanical properties and biological responses *in vitro*. *Materials* 13 (11), 2589. doi:10.3390/ma13112589

Lu, Y., Cui, Z., Cheng, L., Li, J., Yang, Z., Zhu, H., et al. (2020). Quantifying the discrepancies in the geometric and mechanical properties of the theoretically designed and additively manufactured scaffolds. *J. Mech. Behav. Biomed. Mater.* 112, 104080. doi:10.1016/j.jmbbm.2020.104080

Melchels, F. P., Barradas, A. M., van Blitterswijk, C. A., de Boer, J., Feijen, J., Grijpma, D. W., et al. (2010). Effects of the architecture of tissue engineering scaffolds on cell seeding and culturing. *Acta biomater.* 6 (11), 4208–4217. doi:10.1016/j.actbio.2010.06.012

Memon, A. R., Wang, E., Hu, J., Egger, J., and Chen, X. (2020). A review on computer-aided design and manufacturing of patient-specific maxillofacial implants. *Expert Rev. Med. devices* 17 (4), 345–356. doi:10.1080/17434440.2020.1736040

Milovanovic, J. R., Stojkovic, M. S., Husain, K. N., Korunovic, N. D., and Arandjelovic, J. (20202020). Holistic approach in designing the personalized bone scaffold: The case of reconstruction of large missing piece of mandible caused by congenital anatomic anomaly. *J. Healthc. Eng.* 2020, 1–13. doi:10.1155/2020/6689961

Novaes Jr, A. B., Jr, Souza, S. L. S. d., Barros, R. R. M. d., Pereira, K. K. Y., Iezzi, G., Piattelli, A., et al. (2010). Influence of implant surfaces on osseointegration. *Braz. Dent. J.* 21 (6), 471–481. doi:10.1590/s0103-64402010000600001

Pei, X., Zhang, B., Fan, Y., Zhu, X., Sun, Y., Wang, Q., et al. (2017). Bionic mechanical design of titanium bone tissue implants and 3D printing manufacture. *Mater. Lett.* 208, 133–137. doi:10.1016/j.matlet.2017.04.128

Pei, X., Wu, L., Zhou, C., Fan, H., Gou, M., Li, Z., et al. (2020). 3D printed titanium scaffolds with homogeneous diamond-like structures mimicking that of the osteocyte microenvironment and its bone regeneration study. *Biofabrication* 13 (1), 015008. doi:10.1088/1758-5090/abc060

Perrin, D., Szmukler-Moncler, S., Echikou, C., Pointaire, P., and Bernard, J. P. (2002). Bone response to alteration of surface topography and surface composition of sandblasted and acid etched (SLA) implants. *Clin. Oral Implants Res.* 13 (5), 465–469. doi:10.1034/j.1600-0501.2002.130504.x

Rupp, F., Scheideler, L., Rehbein, D., Axmann, D., and Geis-Gerstorfer, J. (2004). Roughness induced dynamic changes of wettability of acid etched titanium implant modifications. *Biomaterials* 25 (7-8), 1429–1438. doi:10.1016/j.biomaterials.2003.08.015

Song, P., Hu, C., Pei, X., Sun, J., Sun, H., Wu, L., et al. (2019). Dual modulation of crystallinity and macro-/microstructures of 3D printed porous titanium implants to enhance stability and osseointegration. *J. Mat. Chem. B* 7 (17), 2865–2877. doi:10.1039/c9tb00093c

Standard, I. (2011). ISO 13314: 2011 (E)(2011) mechanical testing of metals—ductility testing—compression test for porous and cellular metals. *Ref number ISO* 13314(13314), 1–7.

Stepanovska, J., Matejka, R., Rosina, J., Bacakova, L., and Kolarova, H. (2020). Treatments for enhancing the biocompatibility of titanium implants. *Biomed. Pap.* 164 (1), 23–33. doi:10.5507/bp.2019.062

Tack, P., Victor, J., Gemmel, P., and Annemans, L. (2016). 3D-printing techniques in a medical setting: A systematic literature review. *Biomed. Eng. OnLine* 15 (1), 115. doi:10.1186/s12938-016-0236-4

Vaithilingam, J., Goodridge, R. D., Hague, R. J., Christie, S. D., and Edmondson, S. (2016). The effect of laser remelting on the surface chemistry of Ti6al4V components fabricated by selective laser melting. *J. Mater. Process. Technol.* 232, 1–8. doi:10.1016/j.jmatprotec.2016.01.022

Walker, J. M., Bodamer, E., Kleinfehn, A., Luo, Y., Becker, M., Dean, D., et al. (2017). Design and mechanical characterization of solid and highly porous 3D printed poly(propylene fumarate) scaffolds. *Prog. Addit. Manuf.* 2 (1), 99–108. doi:10.1007/s40964-017-0021-3

Wang, Z., Wang, C., Li, C., Qin, Y., Zhong, L., Chen, B., et al. (2017). Analysis of factors influencing bone ingrowth into three-dimensional printed porous metal scaffolds: A review. *J. Alloys Compd.* 717, 271–285. doi:10.1016/j.jallcom.2017.05.079

Wang, G., Shen, L., Zhao, J., Liang, H., Xie, D., Tian, Z., et al. (2018). Design and compressive behavior of controllable irregular porous scaffolds: Based on voronoi-tessellation and for additive manufacturing. *ACS Biomater. Sci. Eng.* 4 (2), 719–727. doi:10.1021/acsbiomaterials.7b00916

Webster, A. P., and Ross, T. J. (2013). Anodizing color coded anodized Ti6Al4V medical devices for increasing bone cell functions. *Int. J. Nanomedicine* 8, 109–117. doi:10.2147/ijn.s36203

Wei, J., Herrler, T., Dai, C., Liu, K., Han, D., Li, Q., et al. (2016). Guided self-generation of vascularized neo-bone for autologous reconstruction of large mandibular defects. *J. craniofacial Surg.* 27 (4), 958–962. doi:10.1097/scs.0000000000002680

Xing, H., Komasa, S., Taguchi, Y., Sekino, T., and Okazaki, J. (2014). Osteogenic activity of titanium surfaces with nanonetwork structures. *Int. J. Nanomedicine* 9, 1741–1755. doi:10.2147/ijn.s58502

Yan, C., Hao, L., Hussein, A., and Young, P. (2015). Ti-6Al-4V triply periodic minimal surface structures for bone implants fabricated *via* selective laser melting. *J. Mech. Behav. Biomed. Mater.* 51, 61–73. doi:10.1016/j.jmbbm.2015.06.024

Yoo, D. J. (2011). Porous scaffold design using the distance field and triply periodic minimal surface models. *Biomaterials* 32 (31), 7741–7754. doi:10.1016/j.biomaterials.2011.07.019

Yoo, D. (2012). New paradigms in internal architecture design and freeform fabrication of tissue engineering porous scaffolds. *Med. Eng. Phys.* 34 (6), 762–776. doi:10.1016/j.medengphy.2012.05.008

Yoo, D.-J. (2014). Advanced porous scaffold design using multi-void triply periodic minimal surface models with high surface area to volume ratios. *Int. J. Precis. Eng. Manuf.* 15 (8), 1657–1666. doi:10.1007/s12541-014-0516-5

Yu, M., Wan, Y., Ren, B., Wang, H., Zhang, X., Qiu, C., et al. (2020). 3D printed Ti-6Al-4V implant with a micro/nanostructured surface and its cellular responses. *ACS omega* 5 (49), 31738–31743. doi:10.1021/acsomega.0c04373

Zaharin, H. A., Abdul Rani, A. M., Azam, F. I., Ginta, T. L., Sallih, N., Ahmad, A., et al. (2018). Effect of unit cell type and pore size on porosity and mechanical behavior of additively manufactured Ti6Al4V scaffolds. *Materials* 11 (12), 2402. doi:10.3390/ma11122402

Zha, Y., Li, Y., Lin, T., Chen, J., Zhang, S., Wang, J., et al. (2021). Progenitor cell-derived exosomes endowed with VEGF plasmids enhance osteogenic induction and vascular remodeling in large segmental bone defects. *Theranostics* 11 (1), 397–409. doi:10.7150/thno.50741

Zhang, B., Pei, X., Zhou, C., Fan, Y., Jiang, Q., Ronca, A., et al. (2018). The biomimetic design and 3D printing of customized mechanical properties porous Ti6Al4V scaffold for load-bearing bone reconstruction. *Mater. Des.* 152, 30–39. doi:10.1016/j.matdes.2018.04.065

Zhang, R., Zhong, S., Zeng, L., Li, H., Zhao, R., Zhang, S., et al. (2021). Novel Mg-incorporated micro-arc oxidation coatings for orthopedic implants application. *Materials* 14 (19), 5710. doi:10.3390/ma14195710

Zhu, W., Ma, X., Gou, M., Mei, D., Zhang, K., Chen, S., et al. (2016). 3D printing of functional biomaterials for tissue engineering. *Curr. Opin. Biotechnol.* 40, 103–112. doi:10.1016/j.copbio.2016.03.014